Electronic structure of vertically stacked self-assembled quantum disks

Marek Korkusiński and Pawel Hawrylak

Institute for Microstructural Sciences, National Research Council, Ottawa, Canada, K1A 0R6
(Received 18 August 2000; published 23 April 2001)

The electronic structure of vertically stacked self-assembled quantum disks is studied within the effective mass approximation. The energy spectrum is calculated in the adiabatic approximation and using an exact diagonalization technique. The influence of the strain, dot separation, and the magnetic field on the formation of coupled quantum dot levels is discussed.

I. INTRODUCTION

The development of the ''indium-flush'' technique by Wasilewski and co-workers[1] allowed for the fabrication of high-quality vertically stacked quantum disks. The vertically aligned structures are of interest in fabricating quantum dot lasers[2,3] and light storage devices,[4] and for their possible application in quantum computing.[5,6] The quantum computing applications are related to the isospin of an electron,[7] i.e., the analogy between the quantum dot index and two different spin orientations. Recent experiments by Fafard *et al.*[8] on mesas and by Bayer *et al.*[9] on a single stack show clearly the quantization of the lateral motion in each dot and the quantum mechanical coupling in the vertical direction, resulting in the formation of ''molecular'' quantum dot levels. The formation of molecular orbitals in coupled quantum dots has been investigated experimentally[10–14] and theoretically.[7,15–17] In relevant calculations, Fonseca *et al.*[17] modeled stacked pyramids using an effective mass approximation, including strain and piezoelectric potential as local modifications of the conduction band offset. Pryor[16] studied an infinite chain of coupled pyramids using the eight-band Luttinger-Kohn Hamiltonian, incorporating strain via the Bir-Pikus formalism. Both methods involved a discretization of the one-band or multiband Hamiltonian and a numerical diagonalization of the corresponding very large but sparse Hamiltonian matrix.

We present here a simple method of calculation of electronic levels of coupled vertically stacked quantum disks carried out in the effective mass and adiabatic approximations.[18] It leads to analytical formulas and a qualitative understanding of the single-particle spectrum and its dependence on structure parameters. The calculation of electronic levels is augmented by the calculation of strain, responsible for modifications of the height of the barrier,[16,19–21] and the calculation of the effect of the magnetic field perpendicular to the growth direction, which modifies the vertical coupling of quantum dot levels. Results of the adiabatic approximation are tested against exact diagonalization techniques and shown to be a reliable tool.

II. THE MODEL

Figure 1(a) shows the two vertically stacked disk-shaped InAs quantum dots (QD's). Each dot is formed on a wetting layer (WL) of thickness W, and covered by the GaAs barrier material. Both QD's have the same height H (typically 1–2 nm) and the radii R_1 and R_2 (typically 8–12 nm). The distance between the two wetting layers, D, results in a QD tunneling barrier of thickness $D-H$. The difference in the conduction band offsets for the QD and surrounding material gives the confining potential V_0.

The material parameters of QD's and WL's enter through the effective Rydberg $\mathcal{R} = m_e e^4/2\epsilon^2\hbar^2$ and the effective Bohr radius, $a_B = \epsilon\hbar^2/m_e e^2$, m_e and ϵ being the effective mass of an electron and the dielectric constant, respectively. Throughout this work $\mathcal{R}$ and a_B will be used as units of energy and length, respectively.

In cylindrical coordinates the effective mass Hamiltonian of our system may be written as
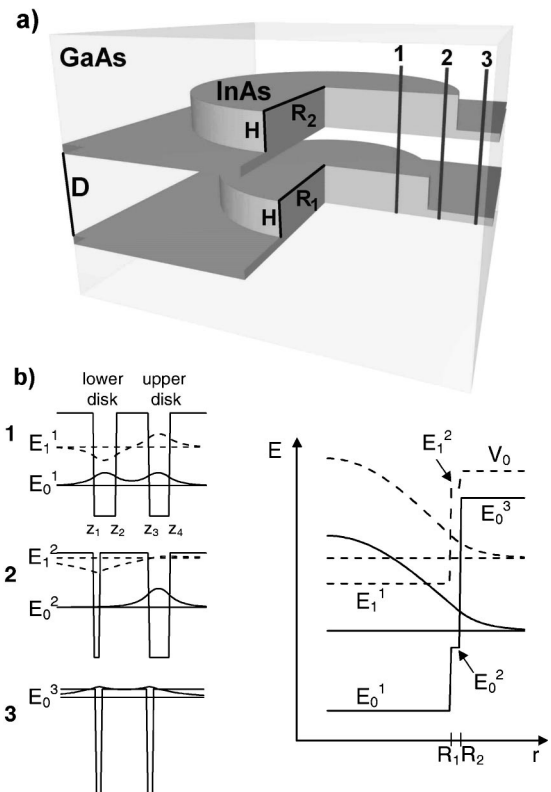

FIG. 1. (a) Schematic picture of the InAs/GaAs double self-assembled quantum dots modeled as disks of radii R_1 and R_2, heights H, and wetting layer separation D; (b) illustration of system potentials in the adiabatic calculation of electronic states (see text).

$$\hat{H} = -\frac{1}{r^2}\left(r\frac{\partial}{\partial r}r\frac{\partial}{\partial r} + \frac{\partial^2}{\partial\theta^2}\right) - \frac{\partial^2}{\partial z^2} + V(r,z), \qquad (1)$$

where the potential $V = -V_0$ inside the WL and QD's and $V = 0$ in the barrier.

Let us first carry out a simple qualitative analysis. We separate the motion in the growth and radial directions. For the former we deal with two coupled quantum wells. Let us denote by E_0 the ground state energy, and by $f_1(z)$ and $f_2(z)$ the corresponding orbitals of each isolated well. For identical disks the wave functions in the z direction can be written in the form of symmetric and antisymmetric linear combinations of the single quantum well orbitals: $f_s(z) = [f_1(z) + f_2(z)]/\sqrt{2}$, $f_{as}(z) = [f_1(z) - f_2(z)]/\sqrt{2}$, and the corresponding eigenenergies are $E_{s/as} = E_0 \mp \Delta/2$, where Δ is the splitting between these levels. The motion in the plane of the disk is quantized, with wave functions corresponding to Bessel functions. For infinite barriers the lateral spectrum can be written in terms of zeros of Bessel functions α_m^n: $E(m,n) = (\alpha_m^n/R)^2$, where R is the radius of the disks, n is the radial quantum number, and m is the angular momentum. The electronic spectrum of the system will then be composed of two ladders of states: the symmetric one, $E_0 - \Delta/2 + E(0,1)$, $E_0 - \Delta/2 + E(1,1)$, ..., labeled as $(m,n,+)$, and the antisymmetric one, $E_0 + \Delta/2 + E(0,1)$, $E_0 + \Delta/2 + E(1,1)$, ..., labeled as $(m,n,-)$. When Δ exceeds the quantization of radial motion a crossing of states with different angular momenta and different subbands occurs.

III. ADIABATIC APPROXIMATION

Since the height of both QD's is much smaller than their radii, the electron motion in the growth direction is strongly confined. Therefore the wavefunction of an electron may be written as $\psi(r,\theta,z) = (1/\sqrt{2\pi})e^{im\theta}g_r^\nu(z)f_m^\nu(r)$, where $g_r^\nu(z)$ is a slowly varying function of r. Qualitatively, we then deal with distinct subbands ($\nu = 0,1,\dots$) related to the vertical motion.

For each angular momentum channel m and each subband index ν the functions $g_r^\nu(z)$ and $f_m^\nu(r)$ satisfy the following set of equations:

$$\left[-\frac{\partial^2}{\partial z^2} + V(r,z)\right]g_r^\nu(z) = E_\nu(r)g_r^\nu(z), \qquad (2)$$

$$\left[-\frac{1}{r^2}\left(r\frac{\partial}{\partial r}r\frac{\partial}{\partial r} - m^2\right) + E_\nu(r)\right]f_m^\nu(r) = Ef_m^\nu(r). \qquad (3)$$

The following considerations will be confined to two subbands, $\nu = 0,1$. In each case we first find the energy $E_\nu(r)$ corresponding to the ground ($\nu = 0$) or first excited ($\nu = 1$) states for the vertical motion in the potential $V(r,z)$. The energy $E_\nu(r)$ is then treated as an effective potential for the radial motion [cf. Fig. 1(b)].

As for the vertical motion, we distinguish three regions in our system, as shown in Fig. 1(b). (1) For $r < R_1$ we have two identical quantum wells of width $W + H$, separated by a barrier of thickness $D - H$. In this region, E_0 is the energy of the ground, symmetric state, and E_1 the energy of the first

excited, antisymmetric state. (2) For $R_1 < r < R_2$ we have one narrow quantum well of width W (WL) and one wide quantum well of width $W + H$ (the top QD), separated by a barrier of thickness D. Here, both eigenstates E_0 and E_1 will be mixtures of symmetric and antisymmetric states, and will be larger than their counterparts in the first region. (3) Finally, for $r > R_2$ we have two identical quantum wells (WL's), separated by a barrier of thickness D. The ground, symmetric state E_0 is always confined and lying at a higher energy than the one in the second region, but E_1 for small D may be already above the barrier; in this case we take $E_1 = V_0$. All elements of this approach are schematically shown in Fig. 1(b).

To find the allowed energies $E_\nu(r)$ we employ the transfer matrix formalism.[18] For a given energy E we define the vertical wave function $g_r^\nu(z)$ in five different vertical regions: (i) barrier below the structure, $z < z_1$, $\kappa_1 = \sqrt{-E}$, $g_r^\nu(z) = A_1 \exp[\kappa_1(z - z_1)] + B_1 \exp[-\kappa_1(z - z_1)]$; (ii) first quantum well, $z_1 < z < z_2$, $k_2 = \sqrt{V_0 + E}$, $g_r^\nu(z) = A_2 \exp(-ik_2z) + B_2 \exp(ik_2z)$; (iii) barrier between disks, $z_2 < z < z_3$, $\kappa_3 = \sqrt{-E}$, $g_r^\nu(z) = A_3 \exp(-\kappa_3z) + B_3 \exp(\kappa_3z)$; (iv) second quantum well, $z_3 < z < z_4$, $k_4 = \sqrt{V_0 + E}$, $g_r^\nu(z) = A_4 \exp(-ik_4z) + B_4 \exp(ik_4z)$; (v) barrier above the structure, $z > z_4$, $\kappa_5 = \sqrt{-E}$, $g_r^\nu(z) = A_5 \exp[\kappa_5(z - z_4)] + B_5 \exp[-\kappa_5(z - z_4)]$.

The wave function $g_r^\nu(z)$ must be continuous and smooth at each interface. These conditions allow to write the coefficients A_1, B_1 in terms of A_5, B_5:

$$A_1 = T_{11}(E)A_5 + T_{12}(E)B_5,$$

$$B_1 = T_{21}(E)A_5 + T_{22}(E)B_5,$$

with the transfer matrix defined as

$$T = L^{-1}(\kappa_1, z_1)U(k_2, z_1)U^{-1}(k_2, z_2)V(\kappa_3, z_2)V^{-1}(\kappa_3, z_3)$$
$$\times U(k_4, z_3)U^{-1}(k_4, z_4)R(\kappa_5, z_4).$$

.

By virtue of the fact that $\kappa_3 = \kappa_5$ and $k_2 = k_4$ and setting $z_1 = 0$, the matrices L, U, V, R are defined as

$$L = \begin{bmatrix} 1 & 1 \\ \kappa & -\kappa \end{bmatrix}; \quad U = \begin{bmatrix} e^{-ikz} & e^{ikz} \\ -ike^{-ikz} & ike^{ikz} \end{bmatrix};$$

$$V = \begin{bmatrix} e^{-\kappa z} & e^{\kappa z} \\ -\kappa e^{-\kappa z} & \kappa e^{\kappa z} \end{bmatrix}; \quad R = \begin{bmatrix} 1 & 1 \\ -\kappa & \kappa \end{bmatrix}. \qquad (4)$$

It is convenient to carry out multiplication of matrices $W = UU^{-1}$ and $B = VV^{-1}$ for each well and each barrier to arrive at more modular and expandable expression:

$$W(k,h) = \begin{bmatrix} \cos(kh) & -\sin(kh)/k \\ k\sin(kh) & \cos(kh) \end{bmatrix}, \qquad (5)$$

$$B(\kappa,d) = \begin{bmatrix} \cosh(\kappa d) & -\sinh(\kappa d)/\kappa \\ -\kappa\sinh(\kappa d) & \cosh(\kappa d) \end{bmatrix}, \qquad (6)$$

where d is the barrier thickness and h is the well width. The transfer matrix can now be written as $T = L^{-1}W_1B_1W_2R = L^{-1}AR$, where $A = W_1B_1W_2$ is the matrix describing our structure. Note that this procedure can be easily adjusted to describe stacks of more than two disks by inserting the appropriate number of matrices W and B into A. We find the allowed energies for the vertical motion by imposing boundary conditions, i.e., $B_1 = 0$ and $B_5 = 0$. Since $B_1 = T_{21}(E)A_5 + T_{22}(E)B_5$, if $B_5 = 0$, we must have $T_{21}(E) = 0$. Hence, by finding zeros of the transfer matrix element $T_{21}(E)$ we find allowed values of energies $E_\nu(r)$ for each radial region of the system.

We may now solve for the radial motion [Eq. (3)] in the effective potential $E_\nu(r)$. This potential is constant in each radial region, with discontinuities (steps) for $r = R_1$ and $r = R_2$ [cf. right hand side of Fig. 1(b)]. This permits us to use again the transfer matrix method. Let us denote the energy we are looking for by E. By virtue of the cylindrical symmetry of the system we will build the radial wave function $f_m^\nu(r)$ in terms of Bessel funcions.

For each zero-dimensional (0D) subband ν the innermost region 1 $[E_\nu(r < R_1)]$ corresponds to a propagating solution; therefore we set $k_1 = \sqrt{E - E_\nu^1}$ and form a propagating wave function $f_m^\nu = A_m^1 J_m(k_1 r) + B_m^1 Y_m(k_1 r)$. In the intermediate region 2 $[E_\nu(R_1 < r < R_2)]$, both ''decaying'' $(E < E_\nu)$ and ''propagating'' $(E > E_\nu)$ states are possible. For the former, we define $\kappa_2 = \sqrt{E_\nu^2 - E}$ and take $f_m^\nu = A_m^2 K_m(\kappa_2 r) + B_m^2 I_m(\kappa_2 r)$, whereas for the latter we define $k_2 = \sqrt{E - E_\nu^2}$ and take $f_m^\nu = A_m^2 J_m(k_2 r) + B_m^2 Y_m(k_2 r)$. The outermost region 3 $[E_\nu(r > R_2)]$ will be a quantum barrier, so $\kappa_3 = \sqrt{E_\nu^3 - E}$ and $f_m^\nu = A_m^3 K_m(\kappa_3 r) + B_m^3 I_m(\kappa_3 r)$.

At each boundary we match the wave function and its derivative to derive the transfer matrix T. This matrix can be now written as $T = C^{-1}(R_1)S(R_1)S^{-1}(R_2)D(R_2)$, where the matrix C corresponds to the interior region 1, the matrix SS^{-1} carries the solution through the region 2, and the matrix D propagates it outwards in the region 3. These matrices are given by

$$C(R_1) = \begin{bmatrix} J_m(k_1 R_1) & Y_m(k_1 R_1) \\ k_1 J_m'(k_1 R_1) & k_1 Y_m'(k_1 R_1) \end{bmatrix},$$

$$D(R_2) = \begin{bmatrix} K_m(\kappa_3 R_2) & I_m(\kappa_3 R_2) \\ \kappa_3 K_m'(\kappa_3 R_2) & \kappa_3 I_m'(\kappa_3 R_2) \end{bmatrix}.$$

The matrix S has to be defined separately for the decaying and propagating solution:

$$S^{dec}(R) = \begin{bmatrix} K_m(\kappa_2 R) & I_m(\kappa_2 R) \\ \kappa_2 K_m'(\kappa_2 R) & x_2 I_m'(\kappa_2 R) \end{bmatrix},$$

$$S^{prop}(R) = \begin{bmatrix} J_m(k_2 R) & Y_m(k_2 R) \\ k_2 J_m'(k_2 R) & k_2 Y_m'(k_2 R) \end{bmatrix}.$$

The zeros of the transfer matrix element T_{21} are the eigenvalues of the system.

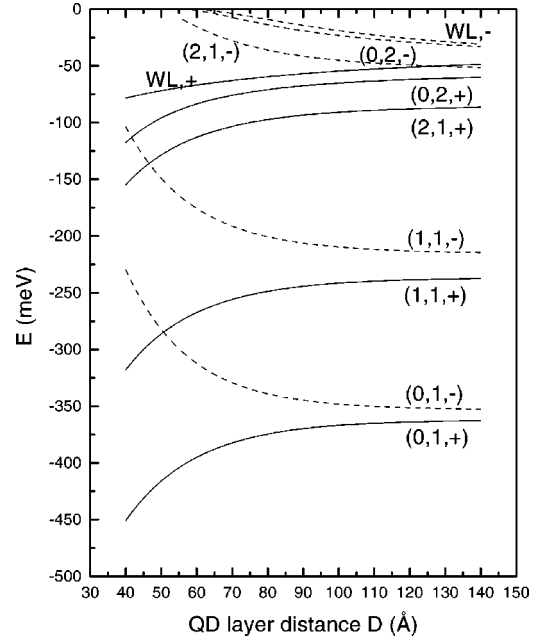Figure 2 shows the dependence of the electronic states on

FIG. 2. Electronic states of the system vs QD layer distance D for disk radii $R_1 = 8$ nm, $R_2 = 8.5$ nm, disk height $H = 2$ nm, barrier height $V_0 = 1$ eV, and the effective mass $m_e = 0.023 m_0$ (ignoring strain) from adiabatic approximation (solid lines, symmetric; dashed lines, antisymmetric). States are labeled by their angular momentum, radial quantum number, and isospin. Symmetric and antisymmetric levels of the double wetting layer system are also shown.

the wetting layer distance D for disk radii $R_1 = 8$ nm and $R_2 = 8.5$ nm, disk height $H = 2$ nm, $V_0 = 1$ eV, and $m_e = 0.023 m_0$. The confining potential corresponds to the band offset between unstrained InAs and GaAs and the mass is that of unstrained InAs (all material constants taken from Ref. 20).

For $D > 6$ nm there are three confined shells, s, p and d, in each dot. The d shell is split into two degenerate states with angular momentum $m = \pm 2$ and one state with angular momentum $m = 0$. When the disks are far apart $(D \approx 14$ nm), for each angular momentum the ''symmetric'' (solid lines) and ''antisymmetric'' (dashed lines) levels are close to each other, and almost degenerate for the s shell. Since the radii of our disks are slightly different, the labels denoting the symmetry of states are only approximate. The lack of symmetry is responsible for the small splitting, of order of $1 - 3$ meV, of the states belonging to the same shell, observed for large D: the higher-energy state contains a greater contribution from the smaller disk, and the lower-energy state from the larger disk. This splitting increases with energy, because the higher the energy the lower the tunneling barrier and the bigger the overlap of wave functions due to their shallower confinement. As the QD's are brought closer together, the splitting between ''symmetric'' and ''antisymmetric'' states grows, reaching about 230 meV for $D = 4$ nm. The most interesting property of this spectrum is the crossing of levels with different symmetry and different angular momentum (in the region $D = 4 - 5.5$ nm).
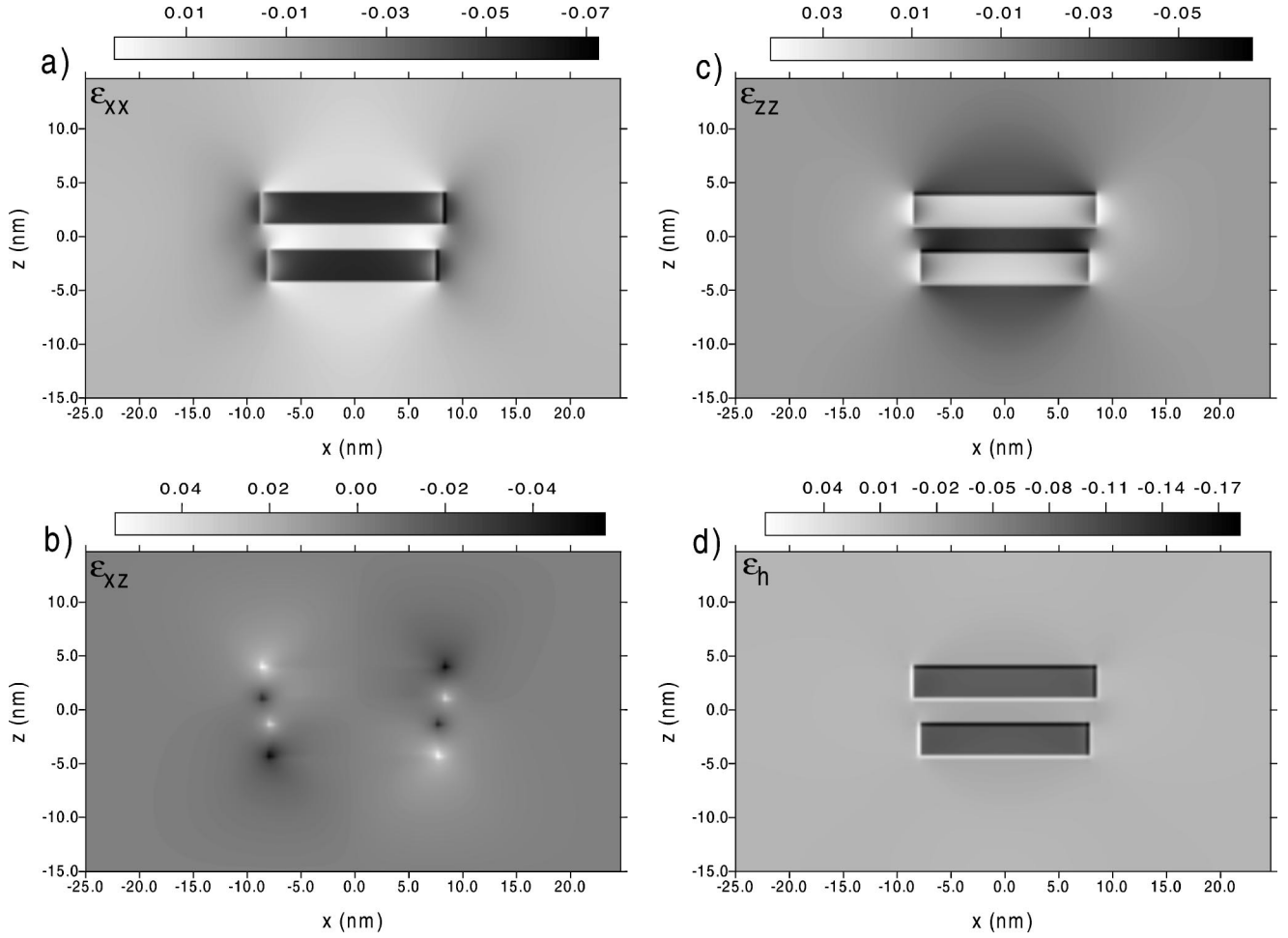
FIG. 3. Vertical cross section of the strain spatial variation through the center of the system (disk height 2 nm, disk radii 8 nm and 8.5 nm): (a) ε_{xx}, (b) ε_{xz}, (c) ε_{zz}, and the hydrostatic strain (d) ε_h. In (a), (c), and (d), compressed areas are white, and expanded areas are dark. Periodic boundary conditions are assumed.

IV. STRAIN, BAND OFFSET, AND EFFECTIVE MASS

A more realistic calculation should account for strain, since it modifies V_0 and the electron effective mass. To take it into account, we use the continuous elasticity theory, discretizing our system on a cubic grid.[16,19,21] This procedure consists of computing the total elastic energy of the system:

$$E = \int d^3r [C_1(\mathbf{r})(\varepsilon_{xx}^2 + \varepsilon_{yy}^2 + \varepsilon_{zz}^2) + C_2(\mathbf{r})$$
$$\times (\varepsilon_{xx}\varepsilon_{yy} + \varepsilon_{xx}\varepsilon_{zz} + \varepsilon_{yy}\varepsilon_{zz}) + C_3(\mathbf{r})$$
$$\times (\varepsilon_{xy}^2 + \varepsilon_{xz}^2 + \varepsilon_{yz}^2) - \alpha(\varepsilon_{xx} + \varepsilon_{yy} + \varepsilon_{zz})], \quad (7)$$

where C_1, C_2, and C_3 are material-specific elastic constants, α is introduced to enforce the lattice mismatch ($\alpha \neq 0$ only in InAs), and ε_{ij} are the strain tensor matrix elements,

$$\varepsilon_{ij}(\mathbf{r}) = \frac{1}{2}\left(\frac{\partial u_i(\mathbf{r})}{\partial x_j} + \frac{\partial u_j(\mathbf{r})}{\partial x_i} \right),$$

and minimizing this energy numerically with respect to displacements of grid nodes $\mathbf{u}(\mathbf{r})$. As a result, we obtain the strain tensor matrix elements ε_{ij} calculated locally for each node. In Fig. 3 we present spatial variation of strain tensor elements ε_{xx} [Fig. 3(a)], ε_{xz} [Fig. 3(b)], ε_{zz} [Fig. 3(c)] and the hydrostatic strain $\varepsilon_h = \varepsilon_{xx} + \varepsilon_{yy} + \varepsilon_{zz}$ [Fig. 3(d)], calculated for disk radii $R_1 = 8$ nm, $R_2 = 8.5$ nm, height $H = 2$ nm, and QD layer distance $D = 4$ nm. Both disks are strongly and uniformly compressed along the radial direction [Fig. 3(a)], but expanded along the symmetry axis [Fig. 3(c)]. The hydrostatic compression is strong within disks and almost absent in the barrier area [Fig. 3(d)].

The strain tensor elements are subsequently input into the strain-dependent eight-band $\mathbf{k} \cdot \mathbf{p}$ Hamiltonian.[22] The resulting local band edge energies for the conduction and valence bands are shown in Fig. 4. Changes in the band edge alignment, both for the conduction and the valence band, are concentrated mainly in QD's, since they depend mainly on the hydrostatic strain. In the conduction band the well depth is reduced to about $V_0^{(s)} = 600$ meV, whereas in the valence band the heavy- and light-hole confinement increases. In contrast, the spin-orbit-split band alignment is reversed. The splitting of light and heavy holes is as large as 200 meV and so it is reasonable to treat the top of the valence band in the ''single band'' approximation.
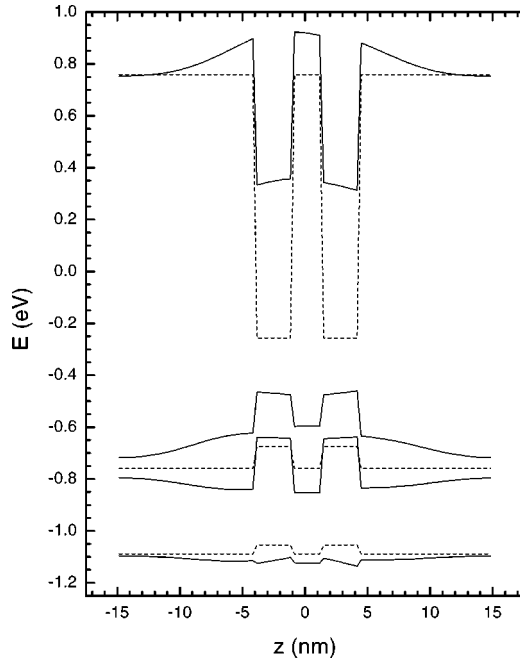
FIG. 4. Band edge alignment along the symmetry axis of the system (dotted lines, unstrained, solid lines, with strain).

Our estimate of $V_0^{(s)}$ is consistent with calculations of Pryor,[16] who calculates the energy spectrum of a quantum wire formed by InAs pyramidal quantum dots of rectangular basis (about 19×19 nm; height about 4 nm), using the Lanczos diagonalization of a discretized Luttinger-Kohn Hamiltonian. Since ground state energies for a circular and a rect-
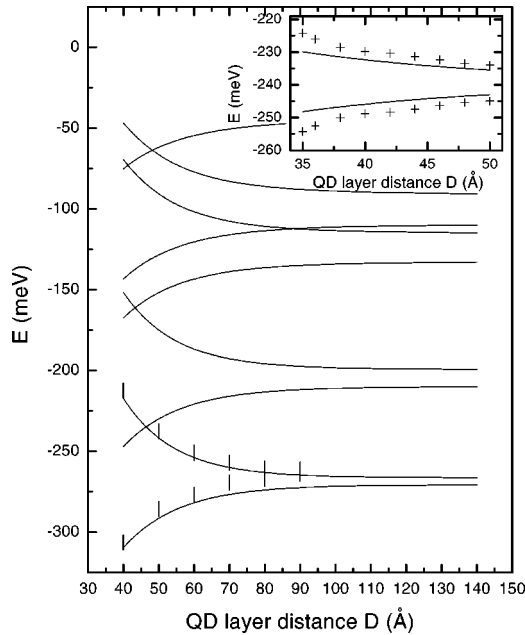

FIG. 5. Electronic levels of the double-dot system for $V_0 = 600$ meV and $m_e = 0.053 m_0$ from adiabatic approximation (solid lines) and exact diagonalization (bars). The inset shows the result of a fitting procedure of electronic levels of our system (solid lines) to Pryor's (Ref. 16, crosses).
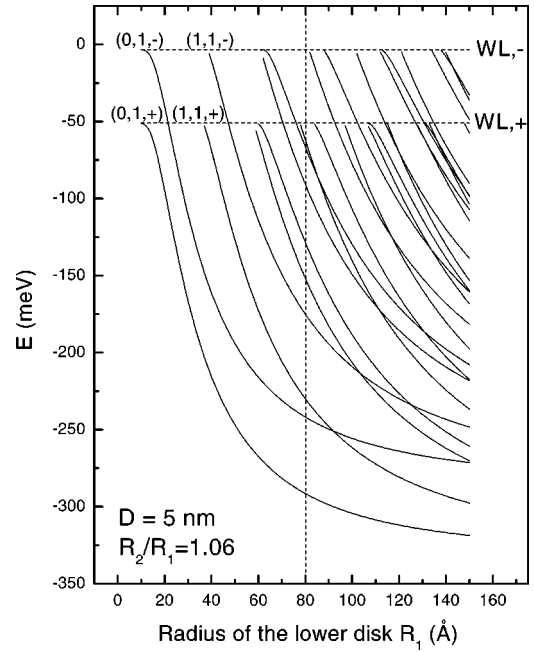

FIG. 6. Dependence of the electronic energy spectrum of the double-dot system on its lateral dimensions (height of both disks $H = 2$ nm, QD layer distance $D = 5$ nm). The ratio R_2/R_1 is kept constant. Dashed line indicates the spectrum shown in Fig. 5.

angular dot with the same basis area are similar (due to localization of the ground state wave function in the center), we compared our electronic spectra with Pryor's, using the electronic effective mass as a fitting parameter. For the s shell we find a good agreement with $m_e = 0.053 m_0$, i.e., an effective mass between that of InAs and GaAs, as expected. The results of fitting to Pryor's calculations are shown in the inset to Fig. 5. Pryor's calculations suggest an effective mass in the InAs strained dot of order of $m_e = 0.04 m_0$, while the far-infaraed (FIR) absorption measurements indicate much higher mass of $0.08 m_0$.[14] Our calculations suggest the use of effective mass $m_e = 0.053 m_0$ but it should be treated as an effective parameter to be obtained by comparison with experiment, e.g., cyclotron resonance.[14]

Figure 5 shows the electronic levels for $V_0 = 600$ meV accounting for strain, and with $m_e = 0.053 m_0$. The dependence of the energy levels on layer distance is unchanged but the symmetric-antisymmetric splitting and the crossing of s and p levels occurs at a different layer separation D.

V. COMPARISON WITH THE RECURSIVE GREEN'S FUNCTION TECHNIQUE

The adiabatic approximation separates the motion in the growth direction and the motion in the lateral direction relying on the disparity of vertical and lateral dimensions of the quantum dot, and on an assumption that the wave function describing the vertical motion, $g_r(z)$, changes slowly along the disk radius. It may be argued that the latter condition is not fulfilled for $r = R_1$ and $r = R_2$, where $g_r(z)$ undergoes a jump, thereby distorting the value of kinetic energy.

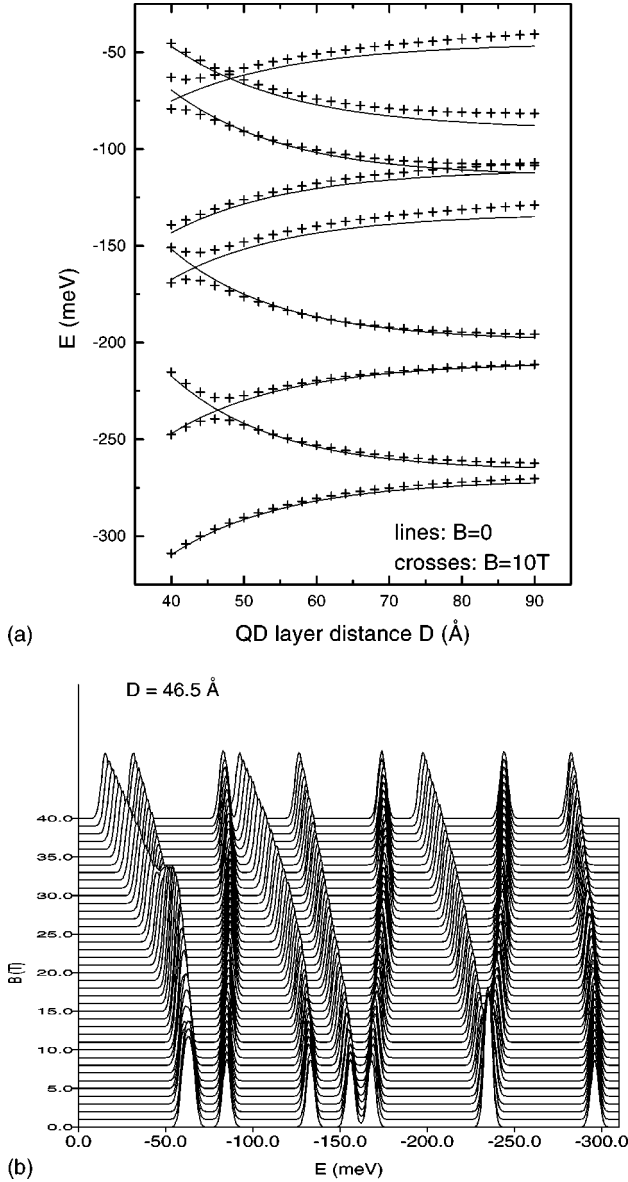We test here the quality of our approach by comparing the

(a)

(b)

FIG. 7. Electronic energy levels in the presence of a parallel magnetic field for the system with $H = 2$ nm, $R_1 = 8$ nm, $R_2 = 8.5$ nm. (a) dependence on the QD layer distance for $B = 0$ (solid lines) and $B = 10$ T (crosses); (b) the density of states for $D = 4.65$ nm in various magnetic fields.

results from the adiabatic model to the values obtained from the recursive Green's function (RGF) calculation of the full three-dimensional Schrödinger equation. The double quantum dot Hamiltonian H, Eq. (1), has been discretized on a cubic grid by replacing the second derivative by the symmetric differences with respect to each coordinate.

In order to minimize the influence of the infinite boundary conditions and the second derivative approximation error, we have chosen the size of the computational box and the discretization length so that our system was divided into about 10^6 cells. The resulting "tight-binding" Hamiltonian matrix has been diagonalized using the RGF technique[23] until convergence was reached. The results for the ground state energy as a function of the quantum dot layer distance are

shown in Fig. 5 (bars). We see that for the s shell the difference between the results of the adiabatic and RGF techniques is of order of only a few meV, so the adiabatic approximation appears to work well for the double quantum dot problem. Due to its discrete nature the RGF method does not capture the influence of the finest structure of the system (i.e., wetting layers) when the tunneling barrier is too large, which results in the systematic shift of the RGF values with the increase of the barier thickness. This shift is not due to the discontinuities in the $g_r(z)$ function, since for large interdisk distances the overall wave function hardly changes with the increase of D, and the resulting distortion in kinetic energy should converge to a constant value. In order to test that, in our model we artificially eliminated the influence of the wetting layers, setting the most outer part of the effective radial potential to be equal to the band offset, and obtained a much better correspondence to the RGF result. The agreement of RGF and adiabatic calculations is much better also if we consider a single disk, for which the finest structure of the system can be accounted for more reliably.

VI. EVOLUTION OF THE DOUBLE-QD SPECTRUM WITH LATERAL SIZE

Since the disk radii depend on the growth conditions, it is of interest to investigate how the change of the lateral size of the system will influence its electronic spectrum. Figure 6 shows the dependence of the energies of electronic states on the radius of the disk R_1, with a fixed ratio $R_2/R_1 = 85/80$ and the QD layer distance $D = 5$ nm. When R_1 is of the order of the height of each disk (i.e., 2 nm) only one shell, s, is confined. With the increase of the radius the energy gap between the symmetric and antisymmetric orbital of this shell remains constant (about 50 meV), which is due to the fact that the distance between disks is fixed. The same is true for other pairs of states composing higher shells, emerging from the WL continuum as R_1 increases. However, the energy distance between shells is not constant, which leads to crossings of states. So, as can be seen from Figs. 5 and 6, the parameter D determines the broadening of each shell, whereas the disk radii determine the relative energy distance between shells.

VII. TUNING OF THE INTERDOT COUPLING WITH MAGNETIC FIELD

In this section we investigate tuning of the interdot coupling with the magnetic field perpendicular to the growth direction. The magnetic part of the Hamiltonian of our double-QD system in cylindrical coordinates, with a magnetic field along the y direction $\mathbf{B} = (0, B, 0)$ and with the vector potential in a Landau gauge is

$$\hat{H}_B = i \Omega z \left(\cos \theta \frac{\partial}{\partial r} - \frac{\sin \theta}{r} \frac{\partial}{\partial \theta} \right) + \frac{z^2}{l^4} = \hat{H}_B^{(1)} + \hat{H}_B^{(2)}, \quad (8)$$

where $\Omega = \omega_c / \mathcal{R}$, $\omega_c = \hbar e B / m_e c$ is the cyclotron energy, $l = \sqrt{\hbar c / e B} / a_B$ is the magnetic length measured in Bohr radii a_B, and we take $\mathbf{A} = (Bz, 0, 0)$. Since analytical formulas

for the electron wave function, $\psi(r,\theta,z) = (1/\sqrt{2\pi})e^{im\theta}g_r^\nu(z)f_m^\nu(r)$, are known, we write the Hamiltonian $\hat{H} = \hat{H}_0 + \hat{H}_B$ in the basis of these functions and diagonalize it numerically. The $\hat{H}_B^{(2)}$ part acts as an additional parabolic confinement in the z direction and gives nonzero matrix elements only for states with the same angular momenta. The $\hat{H}_B^{(1)}$ part combines states with $m' = m \pm 1$, and leads to anticrossings between these levels. This behavior is visualized in Fig. 7(a), where we present a comparison of the energy levels for $B = 0$ and $B = 10$ T. In Fig. 7(b) we show the density of states of our system with $D = 4.65$ nm, for which in zero magnetic field the antisymmetric s and symmetric p states cross. Since $\hat{H}_B^{(1)}$ is linear in B, the dependence of the energy gap between anticrossing states on the magnetic field is approximately linear.

VIII. CONCLUSION

In conclusion, we use the adiabatic approximation to calculate the electronic energy levels in the vertically coupled double quantum dot system. The procedure, beside geometric parameters of the system, requires knowledge of the band edge discontinuity between the quantum well and the barrier and the electron effective mass. We calculate the former using the continuum elasticity theory, and the latter by comparing the energy spectrum to that obtained from the numerical $\mathbf{k} \cdot \mathbf{p}$ calculation, but treat it as a fitting parameter. The change of the QD layer distance strongly modifies the electronic energies, leading to a splitting (of order of 30 meV for small D) between the symmetric and antisymmetric levels, and causes crossings between levels belonging to different shells. These crossings are removed by a magnetic field perpendicular to the growth direction.

[1] Z.R. Wasilewski, S. Fafard, and J.P. McCaffrey, J. Cryst. Growth **201**, 1131 (1999).

[2] M.V. Maximov, Y.M. Shernyakov, A.F. Tsatsul'nikov, A.V. Lunev, A.V. Sakharov, V.M. Ustinov, A.Y. Egorov, A.E. Zhukov, A.R. Kovsch, P.S. Kop'ev, L.V. Asryan, Z.I. Alferov, N.N. Ledentsov, D. Bimberg, A.O. Kosogov, and P. Werner, J. Appl. Phys. **83**, 5561 (1998).

[3] S. Fafard, Z.R. Wasilewski, C.Ni. Allen, K. Hinzer, J.P. McCaffrey, and Y. Feng, Appl. Phys. Lett. **75**, 986 (1999).

[4] T. Lundstrom, W. Schoenfeld, H. Lee, P.M. Petroff, Science **286**, 2312 (1999).

[5] P. Hawrylak, S. Fafard, and Z.R. Wasilewski, Condens. Matter News **7**, 16 (1999).

[6] G. Burkard, G. Seelig, and D. Loss, Phys. Rev. B **62**, 2581 (2000).

[7] J.J. Palacios, and P. Hawrylak, Phys. Rev. B **51**, 1769 (1995).

[8] S. Fafard, M. Spanner, J.P. McCaffrey, and Z.R. Wasilewski, Appl. Phys. Lett. **76**, 2268 (2000).

[9] M. Bayer, P. Hawrylak, K. Hinzer, S. Fafard, M. Korkusiński, Z. Wasilewski, O. Stern, and A. Forchel, Science **291**, 451 (2001).

[10] R.H. Blick, D. Pfannkuche, R.J. Haug, K. von Klitzing, K. Eberl, Phys. Rev. Lett. **80**, 4032 (1998).

[11] L. Kouvenhoven, Science **268**, 1440 (1995).

[12] G. Schedelbeck, W. Wegscheider, M. Bichler, and G. Abstreiter, Science **278**, 1792 (1997).

[13] D.G. Austing, T. Honda, K. Muraki, Y. Tokura, and S. Tarucha, Physica B **249**, 206 (1998).

[14] R.J. Luyken, A. Lorke, M. Fricke, J.P. Kotthaus, G. Medeiros-Ribeiro, and P.M. Petroff, Nanotechnology **10**, 14 (1999).

[15] Y. Tokura, D.G. Austing, and S. Tarucha, J. Phys. C **11**, 6023 (1999); G. Bryant, Phys. Rev. B **47**, 1683 (1993).

[16] C. Pryor, Phys. Rev. Lett. **80**, 3579 (1998).

[17] L.R.C. Fonseca, J.L. Jimenez, and J.P. Leburton, Phys. Rev. B **58**, 9955 (1998).

[18] A. Wojs, P. Hawrylak, S. Fafard, and L. Jacak, Phys. Rev. B **54**, 5604 (1996).

[19] C. Pryor, J. Kim, L.W. Wang, A.J. Williamson, and A. Zunger, J. Appl. Phys. **83**, 2548 (1998).

[20] C. Pryor, Phys. Rev. B **57**, 7190 (1998).

[21] M. Grundmann, O. Stier, and D. Bimberg, Phys. Rev. B **52**, 11 969 (1995).

[22] T.B. Bahder, Phys. Rev. B **41**, 11 992 (1990).

[23] R. Haydock, *The Recursive Solution of the Schrödinger Equation*, Vol. 35 of Solid State Physics, edited by H. Ehrenreich *et al.* (Academic, New York, 1980).